

## **Final Report:**

### **The relationship between crustal structure and earthquake activity on the central Cascadia continental margin in 3D**

**NEHRP grant G17AP00046  
April 1, 2017-September 30, 2018**

**Anne M. Tréhu  
Oregon State University  
anne.trehu@oregonstate.edu**

**Abstract:** A 3D velocity model for the central Oregon margin based on amphibious controlled source data acquired in 1989, 1996 and 2012 indicates the presence of a high velocity slab within the upper plate that generates travel-time anomalies of up to 1.5 s that vary with azimuth for a give source-receiver distance. This complexity is added to the strong 2D heterogeneity characteristic of a submarine subduction zone, in which the subducting plate deepens rapidly between the deformation front and the coastline and the upper plate velocity increases as the accretionary prism abuts (and may be thrust under) the crystalline basement of the forearc. In this study we explored the effect of this heterogenous crustal structure on the precision and accuracy of hypocenters determined using simplified crustal structures and linearized inversion methods by locating synthetic earthquakes for which travel times were generated for the 3D velocity model. We show that apparent depths for earthquakes located in a velocity model appropriate for the Coast Ranges (where most stations are located) are likely overestimated by 10s of km, even if the linearized solutions fit the data better than then those for a velocity model appropriate for the source region of the earthquakes. We also show that addition of even a few offshore stations greatly improve the accuracy of epicenter determinations but that more accurate velocity models are key to obtaining accurate depths. Finally, we discuss preliminary evidence that approximating heterogenous crustal structure by using multiple regional 1D velocity profiles is not adequate for determining depth with the accuracy needed to understand the relationship between interplate and intraplate deformation in a region of strong lateral heterogeneity.

## 1. Motivation:

The Cascadia Subduction zone is exceptional in its low level of instrumentally recorded seismicity, although the presence of an active volcanic arc, the historical and paleoseismic evidence for large plate boundary earthquakes in the past, and seismic images of subsurface structure all clearly indicate that it is a subduction zone. Considering only earthquakes in the ANSS Comprehensive Catalog (ComCat) with  $M > 3$  since 1989, an ~500-km long stretch of the offshore forearc between  $\sim 43^\circ$  and  $48^\circ\text{N}$  has been devoid of earthquakes except for clusters of seismicity between  $\sim 44^\circ$  and  $45^\circ\text{N}$  (Fig. 1a). Lowering the threshold for inclusion to  $M2$  and looking offshore between  $43^\circ\text{N}$  and  $47^\circ\text{N}$ , distributed seismicity is observed within the offshore forearc (Fig. 1b), although the majority of the earthquakes are within two distinct clusters near the events with  $M > 3$ . In recent years, events in this region have been reported by PNSN at a rate of  $\sim 6/\text{year}$ , and template matching (Morton et al., 2018) has identified many additional earthquakes in these clusters. Depths reported in the ANSS catalog for these events are quite scattered, and a distinct separation between crustal and upper mantle is only apparent onshore (Fig. 1c). Relocations that include a velocity model appropriate for the continental shelf and ocean bottom seismometer data, however, suggest that catalog depths are systematically overestimated (e.g. Williams et al., 2012; Tréhu et al., 2015; Stone et al., 2018; Morton et al., 2018; Fig. 1d,e). Systematic overestimation of hypocentral depths for offshore subduction zone earthquakes resulting from a combination of no offshore stations and an inadequate crustal model has also been indicated for aftershocks of the 2010 Maule earthquake offshore south-central Chile (Tréhu et al., 2019).

The largest events along the central Oregon segment of the margin were two moderate earthquakes in 2004 ( $M4.8$ ,  $M4.7$ ). Although PNSN reported hypocentral depths of  $\sim 30$  km for these earthquakes, Tréhu et al. (2008) argued that these events were low-angle thrusts located on or near the plate boundary based on regional moment tensor (RMT) analysis combined with raytracing of secondary phases through a 2D velocity model. The RMT solution for the northern event indicates a slip vector that is consistent with that expected from the plate convergence vector predicted by the NUVEL plate motion model and the southern event indicates a slip vector rotated  $\sim 10^\circ$  relative to the expected direction (Fig. 2). Earthquakes with  $M3.8$  (just big enough for RMT analysis) in the southern cluster in 2012 and 2017, however, indicate predominantly thrust mechanisms on more steeply dipping faults at depths similar to the depth of the events in 2004 (Tréhu et al., 2015, 2018), indicating a locally complex geometry for the plate interface and/or intraplate deformation in the overlying plate (Tréhu et al., 2015; Morton et al., 2018). The southern cluster of events may result from interaction between a subducting seamount and the seaward edge of Siletzia as determined based on aeromagnetic data (Fig. 2). Details of the depth distribution and the relationship of these earthquakes to the crustal structure remained poorly understood, with catalogs by Morton et al. (2018) and Stone et al. (2018) indicating a larger range of depths than indicated by relative relocations of selected events reported by Williams et al. (2011) and Tréhu et al. (2015, 2018).

In this report, we focus on this central, seismically active segment of the Cascadia margin between  $44^\circ\text{N}$  and  $45^\circ\text{N}$ , where we have developed a 3D  $V_p$  model based on amphibious

controlled source data acquired in 1989, 1966 and 2012. Our objective is to better understand (1) the impact of highly heterogeneous subduction zone structure, in general, on the accuracy of hypocentral determinations, and (2) the relationship between the earthquake clusters and local geologic structure along this segment of the margin. NEHRP grant G17AP00046 was used to support the following tasks on the path towards achieving this objective.

- An updated version of the velocity model developed by C. Kenyon (2016) for his MS thesis at OSU, including verification of the model based on first arrivals and adding a Moho surface defined by inversion of wide-angle PmP reflection arrival times. This task required more effort than originally anticipated.
- Determination of the apparent location of synthetic earthquakes generated in the 3D model and then located using times observed at PNSN stations with and without inclusion of offshore OOI stations and for 2 different velocity models.
- Analysis of the impact of different 1D velocity models and  $V_p/V_s$  ratios on hypocentral parameters for 2 small earthquakes that were recorded by the dense amphibious network deployed for the 2012 experiment.

## **2. The $V_p$ model:**

The segment of the Cascadia subduction zone between  $\sim 44^\circ$  and  $45^\circ\text{N}$  has been the focus of several controlled source seismic experiments in the past several decades (Fig. 3). In 1989, as a piggy-back on an ODP seismic reflection site survey of the deformation front (MacKay, 1995), we acquired a multichannel seismic reflection (MCS) profile from the Juan de Fuca plate, across the deformation front, to the coast near  $44.8^\circ\text{N}$  (Tréhu et al., 1995). The seismic sources for the MCS profile were also recorded on a linear array of eight ocean bottom seismometers and 10 stations in the Coast Ranges, which recorded energy from diving waves and wide angle reflections to offsets of up to 160 km (USGS Open-File reports 93-317, 93-318). The data were modeled using a forward modeling technique and provided new information on the dip of the subducting plate and on the geometry of the seaward edge of the crystalline forearc basement (Tréhu et al., 1994).

In 1996, a 2<sup>nd</sup> amphibious, large-aperture transect was acquired near  $44.6^\circ\text{N}$ , funded in part by NEHRP (Gedom et al., 2000). Through serendipity, one of the moderate-size earthquakes in and two of the onshore stations that recorded this earthquake were located on this transect, providing an accurate velocity model for predicting arrival times and take-off angles for multiple secondary phase, providing information for narrowly constraining the earthquake depth (Tréhu et al., 2008). The 1996 experiment also included 2 north-south profiles on the continental margin (Gedom et al., 2000), which were used to develop 1D velocity/depth models for locating offshore earthquakes in this region (Williams et al., 2011; Stone et al., 2018; Morton et al., 2018). Several fan shots acquired in 1996 provided a hint at complex 3D velocity structure but did not provide adequate coverage to resolve the structure.

In 2012, with support from the EarthScope and Marine Geology and Geophysics

programs at NSF, we were able to piggyback on the Ridge to Trench program to image the incoming Juan de Fuca plate (Han et al., 2016, 2017, 2018; Canales et al., 2017) by deploying 33 temporary short period station in the Coast Range, supplementing the Ridge to Trench OBS deployment by 6 additional instruments, and adding several coast-parallel lines of airgun shots (Fig. 3). These data unequivocally indicate the presence of strong lateral heterogeneity in the seismic velocity structure of the upper plate, as shown in Fig. 4, where the travel time for crustal P-waves ( $P_g$ ) observed at the same station but from different azimuths can differ by as much as 1.5 s (Fig. 4B). These data were used by graduate student Chris Kenyon to develop a 3D velocity model in the region for an MS thesis defended during winter quarter 2016. As part of this project, OSU post-doctoral associate Kathy Davenport updated this model using additional data (and correcting some data for which a necessary leap second correction had been neglected). Davenport also inverted travel-times of wide angle PmP reflections, which are clearly observed in the data (Fig. 4A,B) to generate a surface interpreted to be the Moho of the subducted Juan de Fuca plate.

Figure 5 shows several horizontal and vertical slices through the preferred model, which contains very large P-wave velocity variations in the upper plate. Perhaps the most striking feature of the subsurface velocity structure is the high velocity slab in upper plate, where  $V_p$  at 8 km below the sea surface is  $\sim 6$  km/s, in contrast to  $V_p$  of  $\sim 4$  km/s at similar depth north and south of this slab. The high velocity slab likely represents dikes that fed the late Eocene volcanics that erupted through Siletzia (Wells et al., 2014) and result in the dramatic topography of Cape Perpetua. Another important feature of the model is deflection of the Moho beneath this high density slab in the upper crust (Fig. 5, 6), which provides a mechanism for estimating the flexural strength of the subducting plate. This observation of the apparent deformation of the lower plate in response to subduction may have implications for interpreting interplate locking in Cascadia (Tréhu et al., in prep.)

For this project, we used the new 3D velocity model to evaluate the impact of velocity structure on offshore earthquake locations to better understand the relationship between earthquake locations and crustal structure. We generated synthetic data from a grid of points within the model, calculated travel times through the 3D model using the software package NonLinLoc ([http://alomax.free.fr/nlloc/soft5.00/NonLinLoc\\_main.html](http://alomax.free.fr/nlloc/soft5.00/NonLinLoc_main.html)). We then relocated those events using station distributions and velocity models typical of those used by PNSN.

Although our initial objective was to provide a correction matrix for events in this region, we decided that the spatial footprint of the 3D model was too limited and computational uncertainties (discovered when comparing the output of different 3D raytracing algorithms) were too large to provide a definitive correction matrix for offshore earthquakes at this time. As a result of ambitious new data acquisition planned for summer 2020, the volume of forearc for which a 3D model will be available is expected to increase substantially. None-the-less, the work presented here provides insights into systematic biases in the catalog due to inadequate representation of crustal velocity heterogeneity and into the value of having data from even a few offshore seismic stations.



### 3. Locations of synthetic earthquakes:

NonLinLoc is a widely used software package (e.g. Lomax et al., 2000) for non-linear location of the probability distribution function (PDF) of possible hypocenters within heterogeneous velocity models. It uses a ray-tracing approach developed by Podvin and Lecomte (1991) to calculate travel times for a 3D velocity model to all nodes within the model space from a specified list of receiver positions. It can then rapidly do a grid search to find the PDF of possible source locations that meet specified statistical measures of goodness of fit. If the velocity model is a good representation of the in situ seismic velocities, locations and uncertainties thus determined are more realistic than those determined using simplified models and a linearized inversion approach. It can also be used to calculate travel times from specified synthetic source locations to an array of receivers that can then be inverted using a simplified model and linearized inversion to evaluate the impact of assumed, simplified velocity models. In this section, we discuss results of using travel times calculated in the 3D model for synthetic earthquakes to identify systematic biases due to a linearized source location algorithm using Hypo71 and 1D velocity models corresponding to 1D velocity models typical of the Oregon Coast Range region and of the central Oregon continental margin. Figure 7A shows an EW slice through the velocity model. Figure 7B shows an EW vertical slice through the travel time grid calculated for seismic station COR, and 7C shows a horizontal slice at 10 km depth from the time grid for seismic station RNO.

We generated travel times for synthetic earthquakes located in a grid pattern at 20 km intervals from  $x = -90$  to  $-10$  km and  $y = -60$  to  $+40$  relative to the 3D  $V_p$  and Moho model presented in the previous section. All synthetic sources were placed at a depth of 10 km in the velocity model. The synthetic source grid and the stations for which times were calculated are shown in map view in Figure 8A. Synthetic sources located in the vicinity of the earthquake clusters on the central Cascadia margin (Fig. 1,2) are indicated by the blue circle. Stations were chosen to approximate the station distribution available around 2012 with the addition of three offshore stations. The offshore stations include two sites on the OOI cable that have been instrumented with seismometers and a third site closer to shore near Cascadia Initiative station J25 and where the OOI cable has a node that could be instrumented with seismometers if funding became available. No noise was added to the travel times, although times were rounded to the nearest 0.01 s for earthquake location, inducing a nominal (and quite conservative) picking error of  $\sim 0.005$  s. Numerical noise resulting from the 200 m grid spacing of the velocity model also contributes to noise in the synthetic data.

Figure 8B shows locations obtained when the amphibious network was used for locating earthquakes assuming a 1D velocity model similar to the model used by PNSN for the central Oregon Coast Ranges. Figure 8C shows locations obtained when only onshore stations were used for the locations. The differences between the latitude of the synthetic source and the latitude determined with Hypo71 for the 1D velocity model are shown in Figure 8D, and differences for longitude are shown in Figure 8E. Figures 8F and 8G show the hypocentral depths as a function of longitude for the solutions using the

amphibious and onshore networks, respectively. Parameters for the Hypo71 solutions are given in Table 1. The reference depth in the model was set at sea-level, and station elevations above sea-level were treated as station delays (and as negative delays for seafloor stations) when locating the synthetic events using Hypo71.

When even sparse OBS data are available, epicenter mislocations are generally  $<5$  km for all events except for those near the edges of the network (Fig. 8D), although apparent depths show considerable random scatter and a strong overall bias towards deeper depths (average apparent depth = 28.15 km). When no OBSs are available, however, Hypo71 epicenters show a strong bias towards the coast, which increases rapidly as distance from the coast increases (Fig. 8E). With onshore stations only, apparent hypocentral depths are also too deep for most events, and a slight seaward trend in deepening is observed. A similar pattern was noted in depths for earthquakes on the margin reported in the PNSN catalog, although this trend reversed when earthquakes were relocated (Tréhu et al., 2015; Fig. 1E). For nearly all solutions, the rms travel time misfit is  $<0.5$  s, and in many cases, especially for events near the coast ( $X=-10$  or  $-30$ ) it is  $<0.1$  when only onshore stations are used, leading to small nominal horizontal and vertical uncertainties that do not include the biases indicated by the relocations of synthetic events. The average rms travel-time misfit for all events is 0.35 s for the amphibious network and 0.18 s for the onshore only network even though epicenters with the amphibious network are more accurate.

*Caveat: The strong landward bias of events near the deformation front in this simulation in part by the limited aperture of the 3D model, which controlled out selection of stations. Most events occurring far offshore that are located only with onshore stations are large enough magnitude that they are recorded on stations north and south of those that fall within the footprint of the 3D model. These stations would provide additional azimuthal coverage, which should decrease the bias. We have not yet tested this situation explicitly.*

The results when a velocity model appropriate for the continental margin similar to the model used by Williams et al. (2011), Tréhu et al. (2015), Morton et al. (2018) and Stone et al. (2018) is used for locating the synthetic earthquakes are shown in Figure Y. Epicenters when offshore data are included are similar to the actual epicenters and depths are shallower, although quite scattered. When only onshore data are used, the strong bias towards the coast is not observed, and depths for many events do not change from the initial depth. The average rms travel-time misfit for all events is 0.26 s for the amphibious network and 0.24 for the onshore only network.

Several conclusions can be drawn from this exercise.

- Using an appropriate velocity model is critical for obtaining accurate hypocenters for offshore earthquakes in subduction zone and that source depth, in particular, is strongly affected by the velocity model. This result is consistent with the results of several prior studies, although the very strong landward bias when only onshore stations are used with a velocity model corresponding to coastal structure is new. It has probably not been

recognized in previous studies in Cascadia in part because of the very limited and clustered location of recorded seismicity. Another factor influencing this result is the limited aperture of the 3D model used for this exercise, which controlled our selection of stations. Most events occurring far offshore that are located with onshore stations are likely large enough that they are recorded on stations north and south of those that fall within the footprint of the 3D model; these additional observations would increase azimuthal coverage, which should decrease the bias. We have not yet tested this situation explicitly but plan to explore it using a simpler, generic 2D model of subduction.

- The addition of even sparse data offshore is useful for counteracting the shoreward bias in epicenters even when a coastal velocity model is used. Depth, however, remain poorly resolved and strongly biased to deeper depths when a velocity appropriate for the Coast Range is used for locating offshore earthquakes.
- When a velocity model appropriate for the continental shelf is assumed, both the strong shoreward bias in the epicenters and the bias towards greater depth disappear. Depths, however remain very scattered, with a scatter that far exceeds the nominal linearized depth error. This results leads us to ask whether the broader depth range for earthquakes in the central clusters reported by Morton et al. (2018) and Stone et al. (2018) when compared to the depth range represented by the more limited number of events studied in detail by Williams et al. (2011) and Tréhu et al. (2008, 2015, 2018) is real or an artifact of underestimated depth uncertainties. Preliminary evidence that more analysis is needed to address this question is presented below.
- Misfits from a linearized inversion do not reflect these biases and can be much smaller than the bias. For our exercise of locating synthetic earthquakes generated for a 3D velocity model, the best fits were obtained with onshore stations and an onshore velocity model. In this case, the misfit increased when stations were added in the ocean, probably because of the mismatch between the local velocity structure in the vicinity of the ocean stations compared to the velocity model used. In contrast, when a continental margin structure was assumed, the misfit was similar for both the amphibious and onshore-only cases, likely because the continental margin structure was somewhere between the structure beneath the ocean and onshore stations. *[note: While it is generally preferable to use regionalized 1D velocity models, as was done by Stone et al. (2018) and Morton et al. (2018), we used a single 1D model for different tests in order to isolate effects of station distribution from effects of the velocity model.]*

#### **4. Locations of three small earthquakes that occurred during the OR2012 experiment:**

Two small earthquakes occurred in the northern cluster (Fig. 2) on June 28 and 30 and were recorded across the temporary network. These events were also reported by PNSN as well as by Morton et al. (2018). A smaller event occurred in the (generally more seismically productive) southern cluster on June 12 that was only recorded on a subset of the temporary stations and not reported by PNSN. Because 40 temporary 3-component stations were on the Coast Range or on the seafloor within ~100 km of the epicenter when these events occurred, they provide a good test of the location capability of a dense amphibious network and strong constraints on the S-wave velocity in this region. The sensitivity of locations for these two events on the  $V_p/V_s$  ratio and the two P-wave velocity models discussed in the previous section was explored by McKenzie Meyer, a summer 2019 REU student at Oregon State University (Meyer, 2019).

A record sections of the vertical component for the earthquake on June 28, 2012, is shown in Figure 11A. Wadati diagrams (P arrival time versus S-P time) are shown in Figure 11B and C. For both events, the Wadati diagrams indicate a well-constrained  $V_p/V_s$  ratio of 1.77-1.78. This contrasts with a  $V_p/V_s$  ratio of 1.82 derived by Tréhu et al. (2008) and 1.76 derived by Morton et al. (2018). The total number of picks used for the locations was 56-60, with P and S picks possible on only 2 of the OBSs because of high background noise levels and “ringy” data due to poor coupling to the seafloor at some sites (Fig 11B,C). As for the exercise with synthetic earthquake travel times, events were located using Hypo71, using a velocity of 2.5 km/s to calculate station delays onshore based on elevation and a velocity of 1.5 km/s to calculate stations advances for seafloor stations. Figure 12 shows the results of sensitivity tests using the CR and OR3 velocity models and different  $V_p/V_s$  ratios for the events on June 28 and 30; table shows results for all three events.  $V_p/V_s$  ratios of 1.74, 1.77, 1.84 and 1.90 were tested. Morton et al. (2018) also located these events and obtained similar hypocenters. The preferred epicenter for each is shown in Fig. 2.

With only one exception, the minimum residual was obtained for a  $V_p/V_s$  of 1.78, validating the results of the Wadati diagrams, which were determined prior to earthquake location (i.e. with an arbitrary start time for P arrivals). Hypocenter depths were deeper for the coast range model (CR) than for the continental shelf model (OR3) (>20 km compared to 14-15 km). Although the rms misfit was much lower for the CR model (~0.24 s compared to 0.40 s), based on results from the previous section, the depths obtained from the OR3 model are likely more accurate. Because of the large number of stations used for the inversion, the nominal linearized uncertainties in both horizontal and vertical directions are ~1 km, which substantially underestimates the actual uncertainty.

Given the large number of stations, we expected to be able to determine mechanisms from first motions. However, plots of the first motion polarities produced by Hypo71 show a lot of scatter. This may be due to local ray bending due to heterogeneous velocity structure, which can severely distort take-off angles or to polarity conventions that vary from site to site.

## **5. Next steps:**

Our next step with the analysis of these earthquakes is to locate them within the 3D velocity model. This has proved to be more difficult and time-consuming than anticipated because of the need to systematically compare the 3D raytracing/travel-time calculation methods used by NonLinLoc and eTomo (the software used to invert the controlled source observations to obtain the 3D velocity model, Toomey et al., 1994) and test the statistical parameters needed to provide a robust solution with NonLinLoc. A comparison between the travel times predicted for the 3D model with those predicted by the best fit solution for the 1D model shows systematic differences as a function of offset and azimuth, indicating that additional refinement of the hypocenters is needed in order to more precisely and accurately locate the earthquakes relative to the structures.

Additional analysis is also underway to determine mechanisms for the two events from the northern cluster. If robust mechanisms can be determined, they would contribute significant new information about what is driving seismicity at here. Unlike the southern cluster, the reason for seismicity in the cluster remains enigmatic. Tréhu et al. (2012) speculated that it might be due to a deeply subducted seamount that is eroding the base of the upper plate, resulting in a locally deep basin within the larger Newport basin.

Finally, in collaboration with Sue Bilek and Emily Morton, I am currently exploring the question of whether the greater depth range of earthquakes in the Morton et al. (2018) catalog when compared to the results of Tréhu et al. (2018) is real or is due to unreliable uncertainty estimates for linearized location in simplified velocity models. We are focusing on a cluster of 22 earthquakes that occurred on June 25-July 1, 2015 that have depths distributed from 5 to 20 km in the Morton et al. (2018) catalog. Waveforms recorded at the closest station to this cluster, however, show very similar waveforms and nearly identical S-P times that are not compatible with the calculated distance between the station and the hypocenters in the catalog, which predicts a difference of several seconds in the S-P time. We also note that although the Stone et al. (2018) and Morton et al. (2018) catalogs show a similar range in depths for events on the central Cascadia margin (Fig. 1D), results for the depth of individual events that appear in both catalogs are not well correlated (see Fig. DR3 in the supplement to Morton et al., 2018). We plan to combine relative event relocation and absolute location of particularly well-recorded earthquakes within the 3D model to further explore this question. Results of this ongoing analysis will be reported as an addendum to this report as well as in a peer-reviewed publication.

## **6. Conclusions:**

Our results suggest that when locating subduction zone earthquakes, where the crustal thickens rapidly landward and the upper plate velocity varies laterally as the active accretionary wedge abuts against older accreted sediments and crystalline rocks of the forearc basement, hypocenters determined using a land-based network and velocity model appropriate for the coastal ranges will be strongly biased, with hypocentral depths

overestimated by 10s of km, resulting in a potentially misleading relationship between seismicity and structure. Addition of even a few offshore stations greatly improves the accuracy of epicenters, and use of velocity models that more closely represent the offshore velocity structure are critical for removing the bias in depth. In the absence of comprehensive 3D models for the margin, use of multiple 1D based on controlled source experiments models (as implemented, for example, by hypoinverse) addresses the problem of bias but still results in considerable scatter in depth. Preliminary analyses suggest that this scatter, in at least some cases, is not real; it may be due to the relatively poor signal/noise ratio of ocean bottom data in shallow water and travel time uncertainties related to very low velocity marine sediment of variable thickness as well as the shallow depths and consequent lack of stations located within a distance less than the depth for most offshore events. The most accurate locations for clustered events will be obtained by a combination of relative relocation of events within clusters and nonlinear inversion within an accurate 3D velocity model of the events with the largest number of high quality arrival times. In a region of strong lateral heterogeneity, as is observed, on the central Cascadia margin, raytracing in a 3D model may also be needed to determine take-off angles accurately enough to determine mechanisms of small earthquake from first motions.

The analysis presented in this report is clearly over-simplified, and additional work is needed on several fronts. First, we did not have time to fully test the accuracy of the 3D travel-time estimators used both by NonLinLoc or by eTomo and their dependence on grid spacing and other input parameters. We have also assumed a constant  $V_p/V_s$  ratio when converting the 3D  $V_p$  model to a  $V_s$  model even though  $V_p/V_s$  is likely varies significantly within the model (Brocher, 2005). In a later iteration, we may use a  $V_p/V_s$  ratio that depends on  $V_p$  to generate a  $V_s$  model. We have also not had time to fully explore the degree to which independent station corrections for P and S, especially for seafloor stations, has on the precision and accuracy of locations and the degree to which such corrections and/or relative event relocation can compensate for 3D variation in structure. Such efforts, in parallel with ongoing efforts to develop a high-resolution 3D velocity model for Cascadia, should eventually lead to a revised earthquake catalog for the Cascadia margin. In the meantime, hypocenter depths obtained using onshore velocity models in the source region of offshore earthquakes are suspect; even when multiple 1D models are used, linearized estimates of depth uncertainties are suspect.

## References:

- Brocher, T. M. (2005). Empirical Relations between Elastic Wavespeeds and Density in the Earth's Crust. *Bulletin of the Seismological Society of America*, 95(6), 2081–2092
- Canales, J. P., Carbotte, S. M., Nedimović, M. R., & Carton, H. (2017). Dry Juan de Fuca slab revealed by quantification of water entering Cascadia subduction zone. *Nature Geoscience*, 10(11), 864–870.
- Gerdorf, M. A.M. Trehu, E. R. Flueh, D. Klaeschen, The continental margin off Oregon from seismic investigations, *Tectonophysics*, v. 329, p. 79-97, 2000.
- Han, S., Carbotte, S. M., Canales, J. P., Nedimović, M. R., Carton, H., Gibson, J. C., & Horning,

- G. W. (2016). Seismic reflection imaging of the Juan de Fuca plate from ridge to trench: New constraints on the distribution of faulting and evolution of the crust prior to subduction. *Journal of Geophysical Research: Solid Earth*, 121(3), 1849–1872.
- Han, S., Bangs, N. L., Carbotte, S. M., Saffer, D. M., & Gibson, J. C. (2017). Links between sediment consolidation and Cascadia megathrust slip behaviour. *Nature Geoscience*, 10(12), 954–959.
- Han, S., Carbotte, S. M., Canales, J. P., Nedimović, M. R., & Carton, H. (2018). Along-Trench Structural Variations of the Subducting Juan de Fuca Plate From Multichannel Seismic Reflection Imaging. *Journal of Geophysical Research: Solid Earth*, 123(4), 3122–3146.
- Hayes, G., 2018, Slab2 - A Comprehensive Subduction Zone Geometry Model: U.S. Geological Survey data release, <https://doi.org/10.5066/F7PV6JNV>.
- Hellweg, M., P. Bodin, J.M. Bormann, H. Haddadi, E. Hauksson, K.D. Smith, Regional seismic networks operating along the west coast of the United States of America, SRL, 2020.
- Kenyon, C. B. (2016). A 3-D Tomographic Model of the P-wave Velocity Structure of the Central Cascadia Forearc, MS Thesis, Oregon State University,
- Lomax, A., Virieux, J., Volant, P., and Berge, C., 2000, Probabilistic earthquake location in 3D and layered models: Introduction of a Metropolis-Gibbs method and comparison with linear locations, in *Advances in Seismic Event Location*, Thurber, C.H., and N. Rabinowitz (eds.), Kluwer, Amsterdam, 101-134
- MacKay, M.E. (1995) Structural variation and landward vergence at the toe of the Oregon accretionary prism, *Tectonics*, v. 14, p. 1309-1320.
- McCrory, P. A., Blair, J. L., Waldhauser, F., & Oppenheimer, D. H. (2012). Juan de Fuca slab geometry and its relation to Wadati-Benioff zone seismicity. *Journal of Geophysical Research: Solid Earth*, 117(B9).
- Podvin, P. and Lecomte, I., 1991, Finite difference computation of traveltimes in very contrasted velocity models: a massively parallel approach and its associated tools., *Geophys. J. Int.*, **105**, 271-284.
- Morton, E.A., S.L. Bilek, C.A. Rowe, Newly detected earthquakes in the Cascadia subduction zone linked to seamount subduction and deformed upper plate, *Geology*, doi/10.1130/G45354.1, 2018.
- Stone, I., J. Vidale, S. Han, E. Roland, Catalog of offshore seismicity in Cascadia: insights into the regional distribution of microseismicity and its relation to subduction processes, *J. Geophys. Res.*, doi:/10.1002/2017JB14966, 2018.
- Tréhu, A.M., I. Asudeh, T.M. Brocher, J. Luetgert, W.D. Mooney, J.L. Nabelek, Y. Nakamura, Crustal architecture of the Cascadia forearc, *Science*, v. 265, pp. 237-243, 1994.
- Tréhu, A.M., Braunmiller, J., Nabelek, J.L., Probable low-angle thrust earthquakes on the Juan de Fuca-North America plate boundary, *Geology*, v. 36, p. 127-130, 2008.
- Tréhu, A.M., Blakely, R.J., Williams, M.C., Subducted seamounts and recent earthquakes beneath the central Cascadia forearc, *Geology*, v. 40, p. 103-106, 2012.
- Tréhu, A. M., Braunmiller, J., & Davis, E. (2015). Seismicity of the Central Cascadia Continental Margin near 44.5 N: A Decadal View. *Seismological Research Letters*, 86(3), 819–829.
- Tréhu, A.M., Wilcock, W.S.D., Hilmo\*, R., Bodin, P., Connolly, J., Roland, E.C., and Braunmiller, J. (2018). The role of the Ocean Observatories Initiative in monitoring the offshore earthquake activity of the Cascadia subduction zone: *Oceanography*, v. 31, p. 104-113.
- Wells, R., Bukry, D., Friedman, R., Pyle, D., Duncan, R., Haeussler, P., Wooden, J. (2014). Geologic history of Siletzia, a large igneous province in the Oregon and Washington Coast Range: Correlation to the geomagnetic polarity time scale and implications for a long-lived Yellowstone hotspot. *Geosphere*, 10(4), 692–719.
- Williams, M.C., Trehu, A.M., Braunmiller, J., Seismicity at the Cascadia plate boundary beneath the Oregon continental shelf, *Bull. Seis. Soc. Am.*, v. 101, p. 940-950, 2011.

### Figure Captions:

Figure 1A. Earthquakes in Cascadia with  $M > 3$  since 1989 in the ANSS comprehensive catalog. Epicenters located between the deformation front and the coast are shown in red. Circles scaled by magnitude. Dashed white line is the seaward edge of Siletzia from magnetic anomaly data. Dashed black line is the  $450^\circ$  isotherm from Wang and Hyndman (1993). B. Earthquakes with  $M > 2$  since 2000 in the ANSS comprehensive catalog. C. Depths of earthquakes in B. Violet line is the plate interface from Slab2.0 (Hayes, 2018) at  $47^\circ$ , red is at  $45^\circ$ , green is at  $43^\circ$ . D. Depths of earthquakes in the central region in the Stone et al. (2018) catalog. Green triangle is the coastline; blue triangle is the deformation front. Plate interface from McCrory et al. (2012). E. Depths of earthquakes between  $44^\circ$  and  $45^\circ$  from Tréhu et al. (2018). Red circles are events that were relocated with depth constrained as discussed in the text. Dark grey circles are PNSN locations for the events shown in red. Light grey circles are catalog events that were not relocated. Plate interface from Gerdom et al. (2000) (equivalent to McCrory et al., 2012).

Figure 2. Aeromagnetic anomalies, earthquake locations and regional moment tensors on the central Cascadia margin (updated from Tréhu et al., 2012, 2015, 2018). SES - seaward edge of Siletzia. SS – subducted seamount. LEV – late Eocene volcanics (Wells et al., 2014). Dots are epicenters with size scaled by magnitude. Colored dots are epicenters that were relocated based on raytracing secondary phases in a 2D velocity model (green; Tréhu et al., 2008), regional moment tensor inversion or location relative to the green events (white documented in Williams, et al., 2011; yellow documented by Tréhu et al., 2015, 2018). Orange dots show the preferred solution for events discussed in section 4;

Figure 3. Locations of airgun shots (lines) and stations (triangles) from 1989 (orange), 1996 (yellow), and 2012 (red) used to develop the 3D Vp model. Only a subset of stations deployed in 1996 were used. The 2D velocity model of Gerdom et al. (2000), based on the entire 1996 data set, was used as a starting model for the 3D model.

Figure 4. Examples of data used for the 3D Vp model. A. Example from the 1996 ORWELL experiment. B. Example from the 2012 Ridge-to-Trench piggyback experiment. Pg and PmP phases are labeled. A possible intra-crustal reflection (PiP) is identified in A, but picks for that phase are patchy and do not appear to define a single regional surface.

Figure 5. Slices from the 3D Vp model. Horizontal slice in 2 km intervals from 4-12 km depth are on the left; NS-oriented vertical slices are on the right. The longitude and depth range shown are delimited by thin red lines on the 4 km and -124.5446 slices, respectively. The coastline (green), seaward edge of Siletzia (grey), late Eocene volcanics (grey dashed) and subducted seamount (red dot) from Figure 3 are shown on the horizontal slices at 6-12 km. Thick grey line on the NS slices is the Moho surface from inverting PmP arrival times. Only parts of the model constrained by data are shown.

Figure 6A. Three different 2D starting models for the Moho surface, viewed as EW



cross-sections. B. NS profiles of the Moho surface solution perpendicular to the sections in A, showing that the deflection in the Moho beneath the high velocity crustal slab does not depend on the starting model. C. Perspective view of the Moho surface.

Figure 7A. Sample EW cross-section through the 3D velocity model used to simulate travel times using NonLinLoc software ([http://alomax.free.fr/nlloc/soft5.00/NonLinLoc\\_main.html](http://alomax.free.fr/nlloc/soft5.00/NonLinLoc_main.html)). Outside of the region constrained by the data used for the 3D inversion, the velocity model is constrained by the 2D velocity model of Gedom et al. (2000). B. EW cross-section through the calculated travel-time volume for seismic station COR. C. Horizontal slice at 10 km depth through the travel-time volume for seismic station RNO. Travel-time volumes were calculated through the 3D Vp model for all stations shown as yellow triangles in Figure 7. These correspond to PNSN stations TOLO, BABR, COR, MPO, RNO, I02D, JEDS, PBO station B031, CI OBS station J25D, and OOI stations HYSB and HYS14.

Figure 8A. Locations of synthetic earthquakes for which P-wave travel times were determined for the 3D velocity model. These times were used as input to Hypo71 using velocity model CR, shown in Figure 6. The results using all stations shown as yellow triangles is shown in b. Results using only onshore stations are shown in c. The difference between the “actual” latitude and the Hypo71 latitude for the cases in b and c is shown in d. The difference between the “actual” longitude and the Hypo71 longitude for the cases in b and c is shown in e. The Hypo71 depths are shown in f for the case in b and in g for the case in c.

Figure 9. Velocity models CR (similar to the model used by PNSN) and OR3 (similar to the model used for the continental shelf by Williams et al. (2011), Tréhu et al. (2015, 2018), Morton et al. (2018) and Stone et al. (2018).

Figure 10. Locations of the synthetic earthquakes in Figure 8A for velocity model OR3. A. Amphibious network. B. Onshore only network. C. Depths for the amphibious network. D. Depths for the onshore network only.

Figure 11. A. Record section for an earthquake on June 28, 2020 that was recorded across the temporary network deployed for the OR2012 experiment. B. Wadati diagram for the June 28 earthquake, showing a well-constrained Vp/Vs ratio of 1.78. Because the plot was made before locating the earthquake, the origin of the P-axis is arbitrary. C. Wadati diagram for the June 30, 2012 earthquake.

Figure 12. Maps showing the sensitivity of the locations for the June 28 and June 30 earthquakes to the assumed crustal model and the Vp/Vs ratio. Colored circles are results including OBS data. Open circles show the shift when OBS data are not used.

**Table Captions:**

Table 1. Hypocenter parameters for the synthetic earthquakes in the CR and OR3 velocity models. Source locations are given in both the geographic and model X-Y coordinates.

Table 2. Hypocenter parameters for 3 small earthquakes that occurred during the OR2012 temporary deployment that were recorded across the amphibious network.

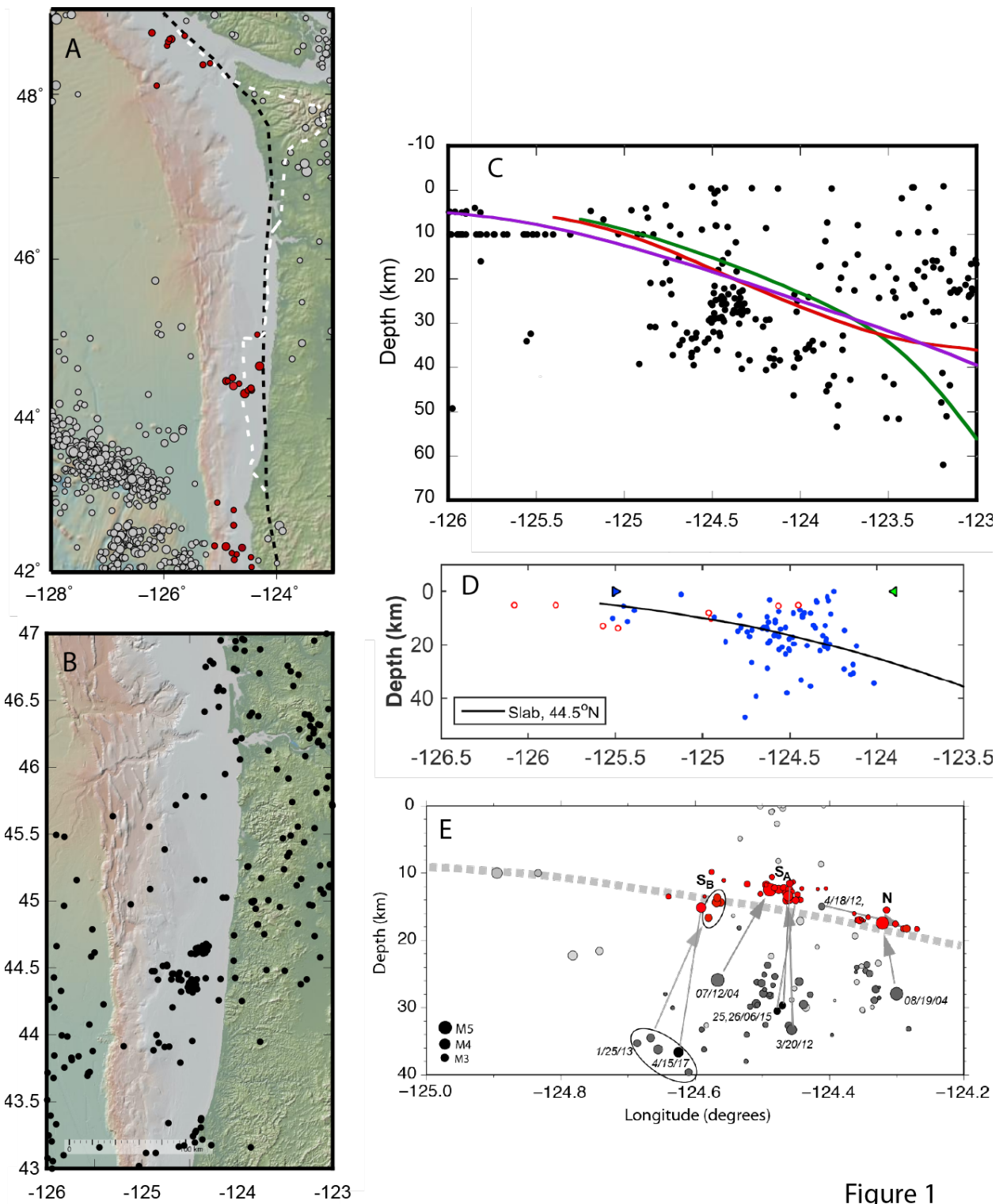


Figure 1

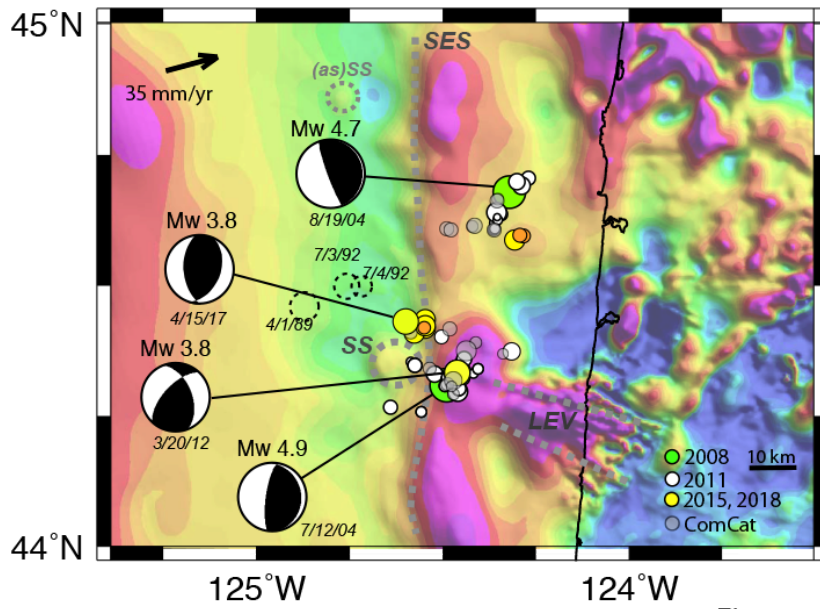


Figure 2

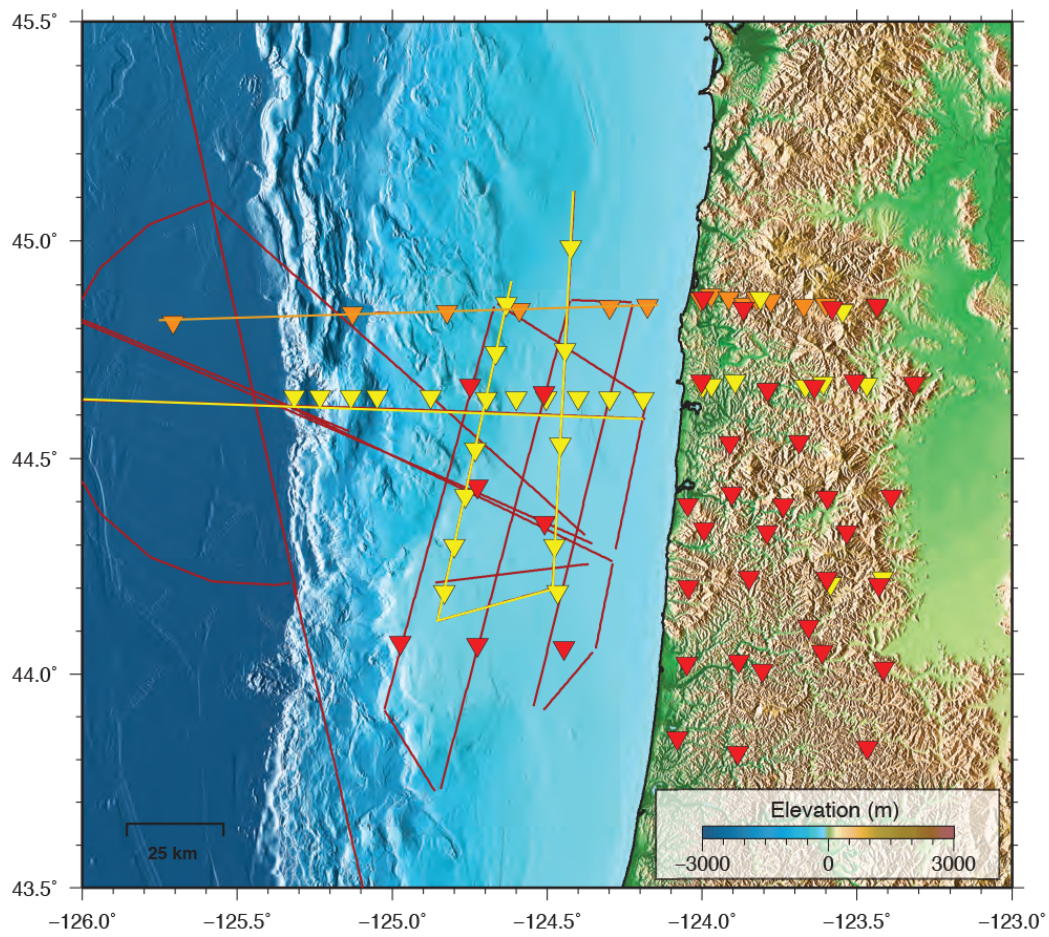


Figure 3

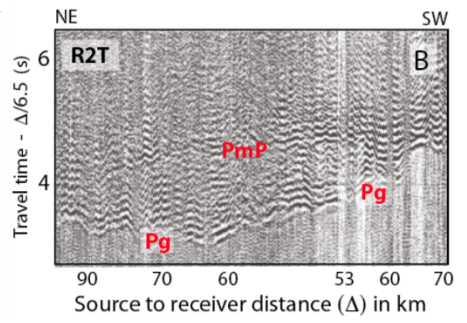
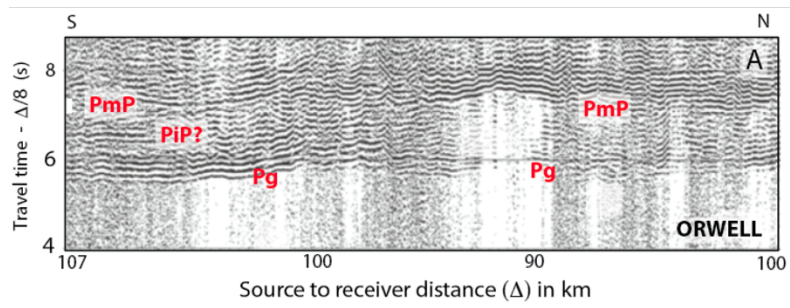


Figure 4



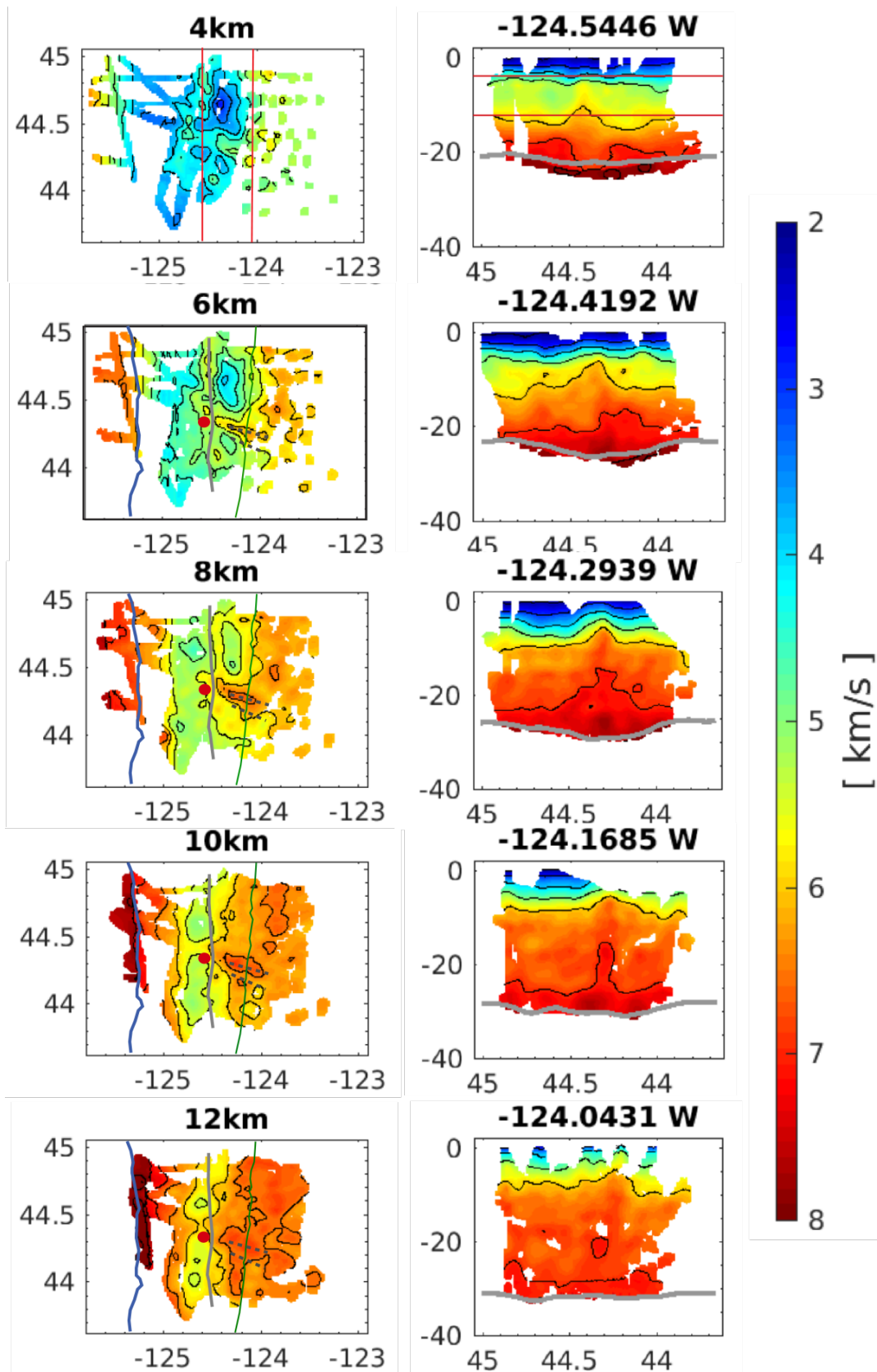


Figure 5

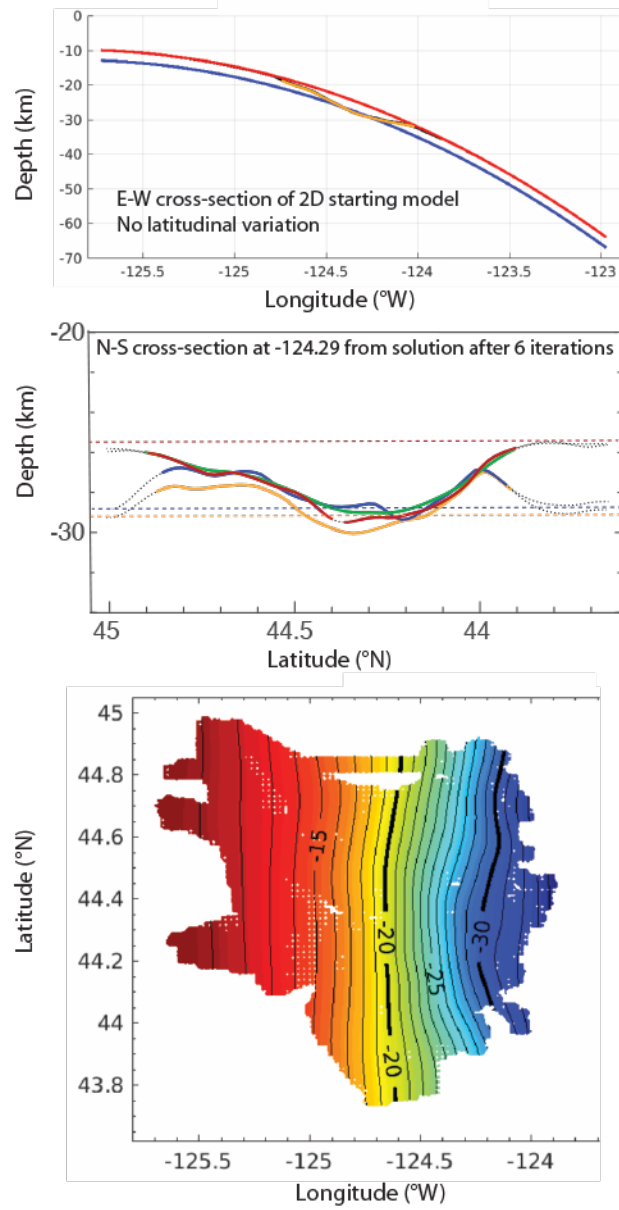


Figure 6

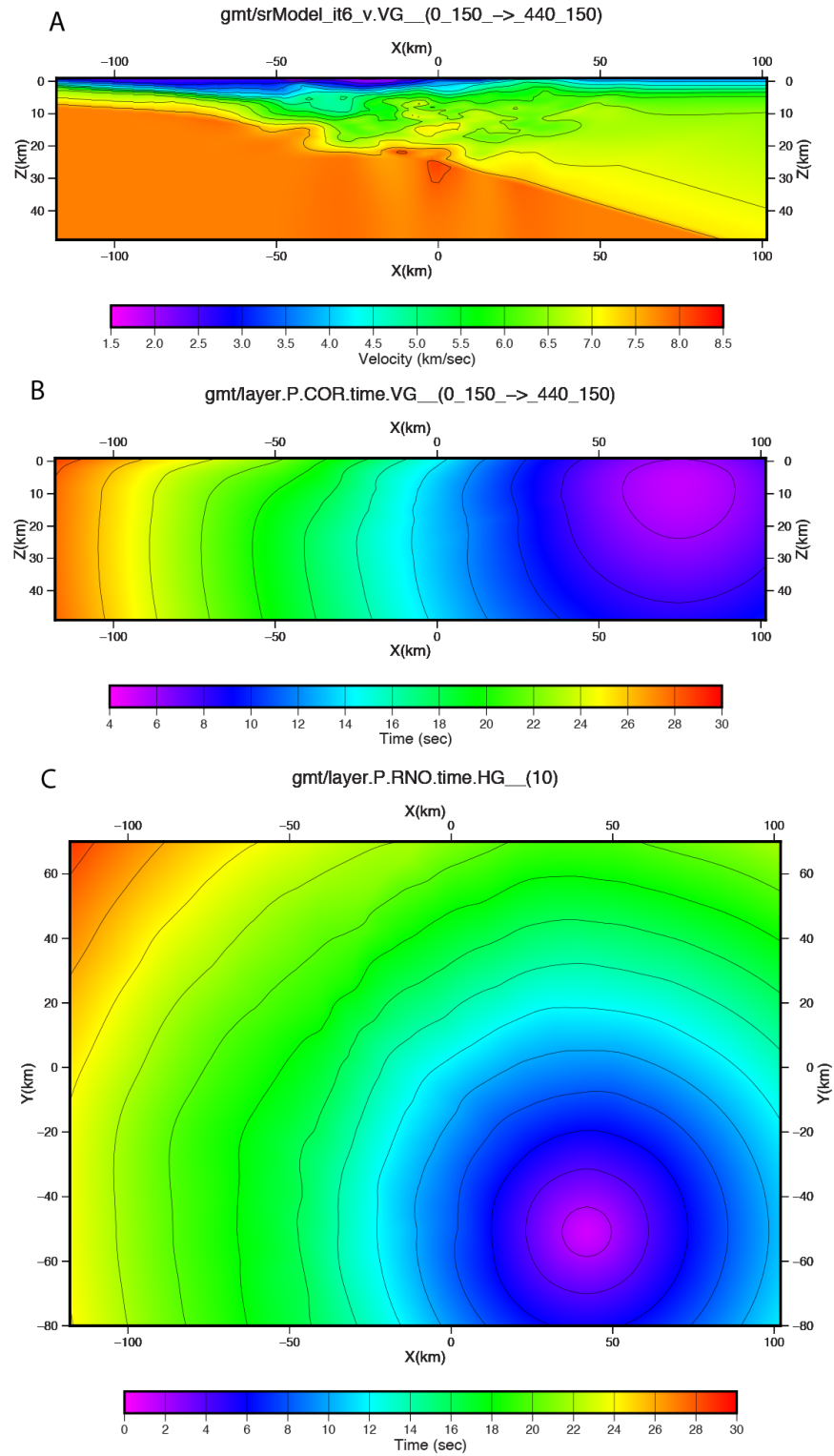


Figure 7



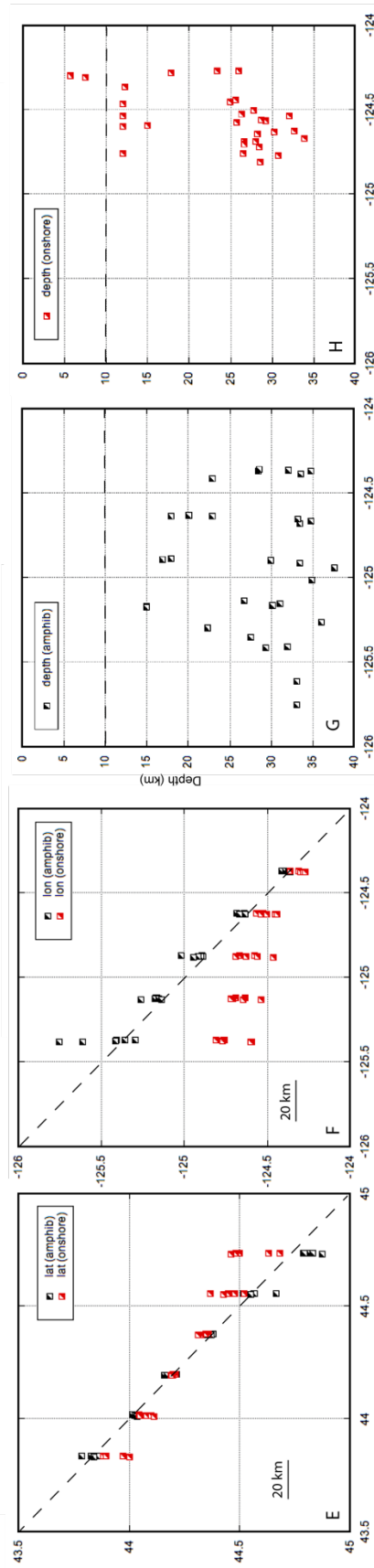
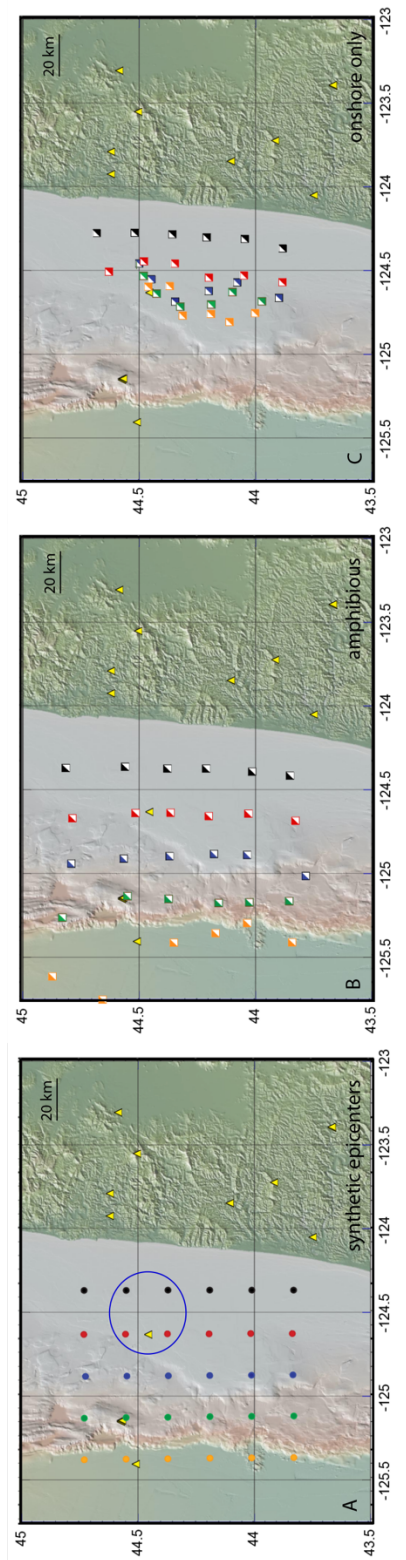


Figure 7

Figure 8

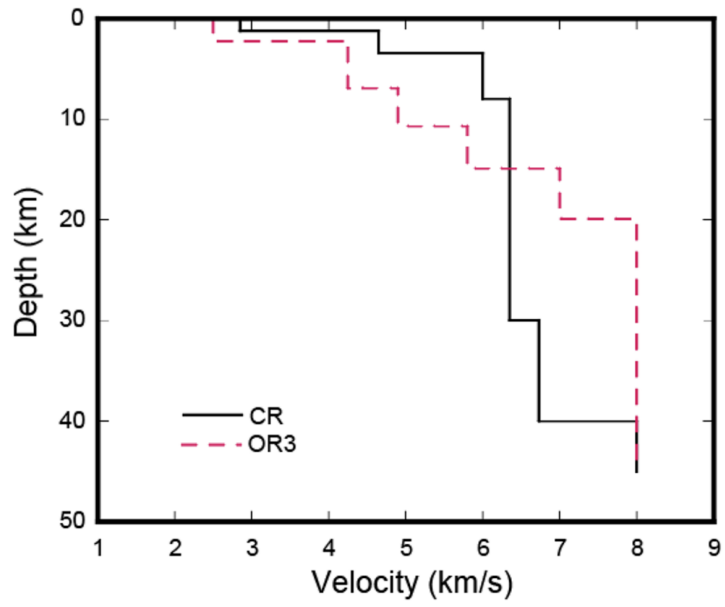


Figure 9

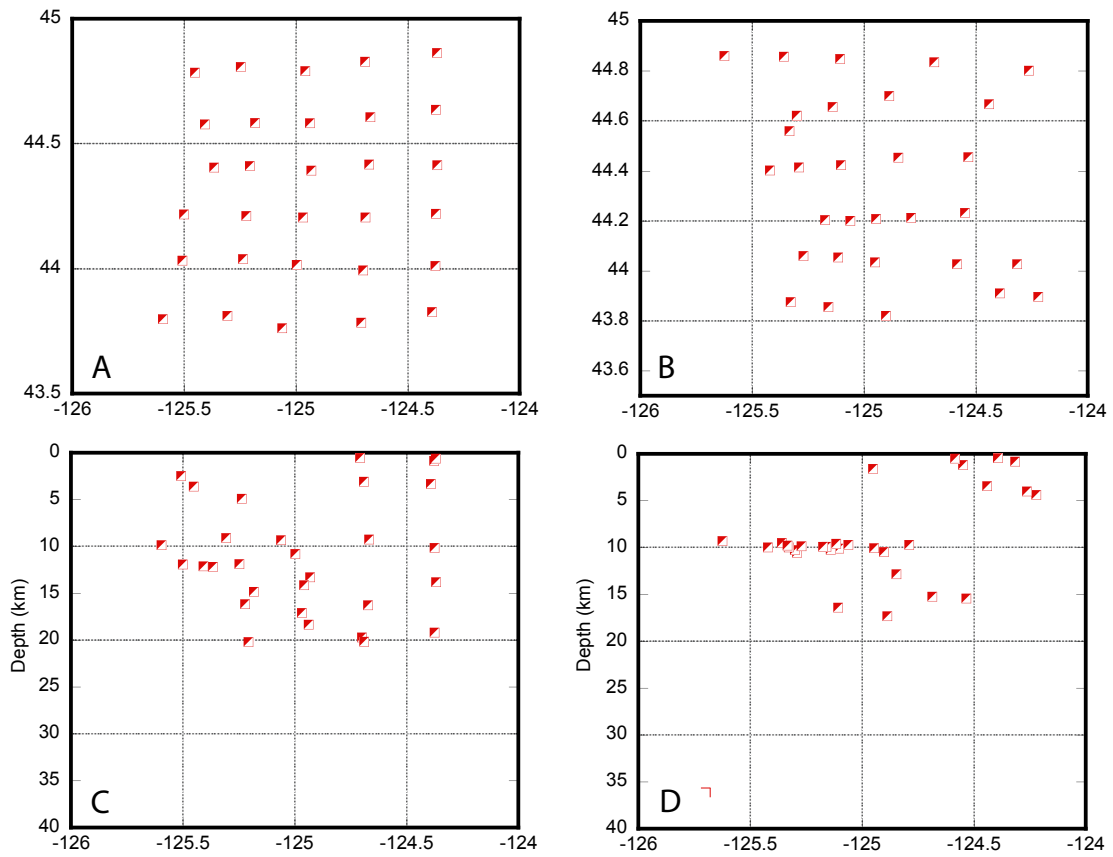


Figure 10

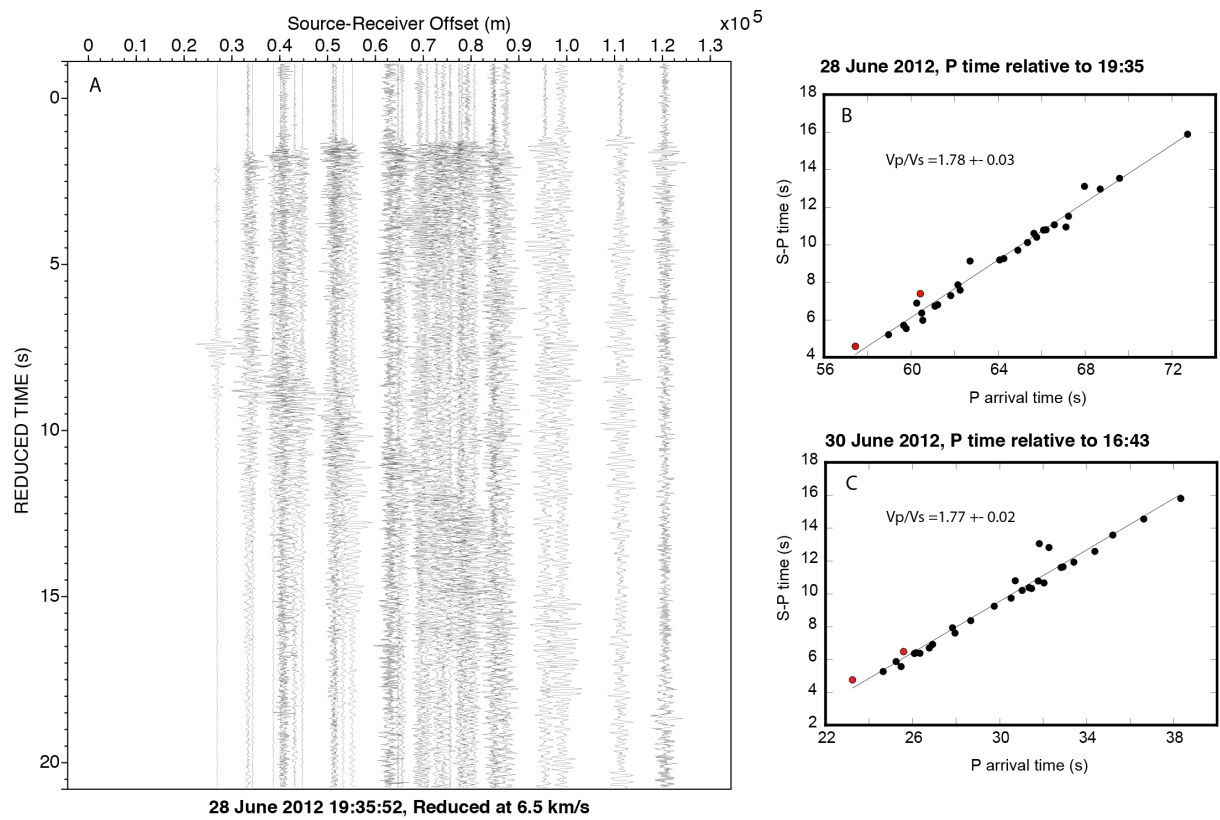


Figure 11

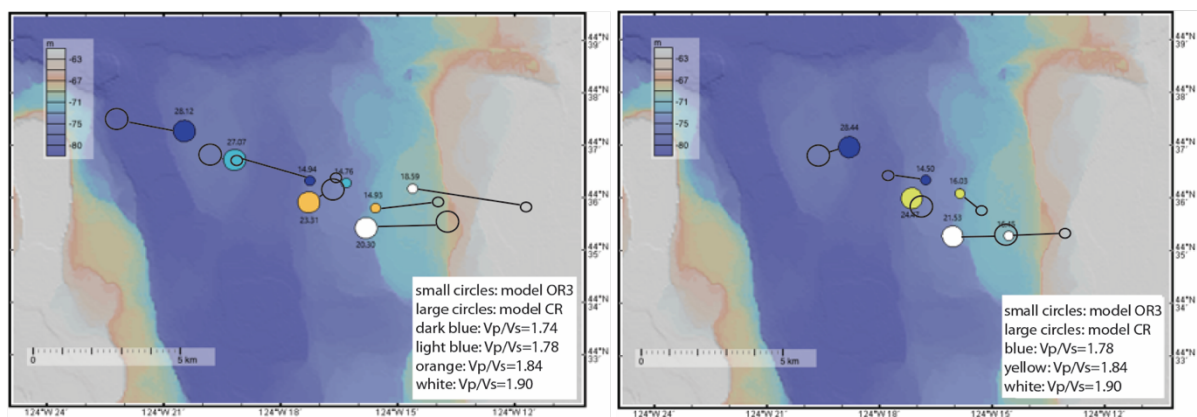


Figure 12

Table 1.

	X position (km)	Y position (km)	Origin Time (s)	Latitude (degrees)	Longitude (degrees)	Depth (km)	Number of phases	Azimuth gap (°)	Minimum distance (km)	rms misfit (s)	horizontal error (km)	vertical error (km)	quality
amphib	-10	-60	-0.92	43.85017	-124.41367	22.91	11	202	31.3	0.4	3.7	10.7	D1
amphib	-10	-40	-1.2	44.01267	-124.389	33.52	11	167	39.9	0.42	3.2	4.5	C1
amphib	-10	-20	-1.08	44.21233	-124.37117	34.81	11	138	34.1	0.3	1.9	2.3	C1
amphib	-10	0	-1.01	44.37833	-124.37083	28.43	11	120	22.5	0.24	1.6	4.7	B1
amphib	-10	20	-0.95	44.56133	-124.35983	28.6	11	168	24.5	0.17	1.4	1.2	C1
amphib	-10	40	-1.68	44.81683	-124.36667	32.11	11	219	41.3	0.37	6	2.8	D1
amphib	-30	-60	-1.34	43.8265	-124.68333	33.45	11	223	51.7	0.38	5	2.7	D1
amphib	-30	-40	-0.51	44.02983	-124.641	17.86	11	188	47.4	0.44	2.2	16.6	D1
amphib	-30	-20	-1.04	44.20083	-124.6545	33.23	11	164	28.5	0.25	1.9	1.9	C1
amphib	-30	0	-0.66	44.366	-124.6355	20.11	11	139	10.1	0.32	2.2	4.2	C1
amphib	-30	20	-0.63	44.51633	-124.63617	22.88	11	160	6.6	0.31	2.3	3.5	C1
amphib	-30	40	-1.46	44.78783	-124.66783	34.83	11	219	36.9	0.25	3.5	1.6	D1
amphib	-50	-60	-2.35	43.7835	-125.0185	34.92	11	243	78.1	0.26	3.9	1.8	D1
amphib	-50	-40	-0.83	44.03567	-124.89367	16.88	11	207	51.3	0.58	1.4	10.3	D1
amphib	-50	-20	-1.02	44.17783	-124.887	17.86	11	186	37.1	0.54	2	10.2	D1
amphib	-50	0	-1.39	44.3685	-124.9	29.94	11	156	23.6	0.19	1.8	1.5	C1
amphib	-50	20	-1.57	44.56583	-124.91483	33.43	11	173	18.9	0.21	2.5	1.3	C1
amphib	-50	40	-2.07	44.79117	-124.944	37.64	11	230	29.3	0.15	2.4	1.2	C1
amphib	-70	-60	-1.79	43.856	-125.16717	30.14	11	247	75.1	0.27	4.4	2.5	D1
amphib	-70	-40	-1.81	44.0265	-125.1735	14.97	11	232	56.8	0.81	2	16.6	D1
amphib	-70	-20	-1.97	44.15867	-125.1775	14.91	11	218	43	0.79	3.6	23.5	D1
amphib	-70	0	-1.91	44.37317	-125.1535	31.02	11	179	22.2	0.3	3.1	2.3	C1
amphib	-70	20	-1.91	44.55017	-125.13633	26.76	11	123	2.8	0.54	5.6	2.7	C1
amphib	-70	40	-3.24	44.83067	-125.26367	36	11	262	30	0.21	4.8	1.8	D1
amphib	-90	-60	-2.15	43.84133	-125.41167	31.92	11	263	74.3	0.21	3.4	1.5	D1
amphib	-90	-40	-1.28	44.03417	-125.29717	22.32	11	243	53.6	0.56	6.6	4	D1
amphib	-90	-20	-1.86	44.17067	-125.35767	27.57	11	240	37.9	0.42	3.9	1.5	D1
amphib	-90	0	-2.29	44.35133	-125.41517	29.35	11	241	17.6	0.4	2.8	1.2	D1
amphib	-90	20	-5.73	44.66367	-125.756	33.07	9	325	32.7	0.06	2.9	0.5	D1
amphib	-90	40	-4.73	44.87317	-125.61483	33.11	9	302	43.7	0.1	4.7	1.5	D1
onshore	-10	-60	-0.05	43.88117	-124.36467	12.27	8	263	29.2	0.08	2.8	5.4	D1
onshore	-10	-40	0.25	44.044	-124.30917	7.49	8	238	38.7	0.1	2.1	142.4	D1
onshore	-10	-20	0.17	44.20917	-124.30067	5.67	8	235	54.8	0.07	1.4	100.3	D1
onshore	-10	0	0.29	44.35667	-124.28133	17.85	8	239	41	0.05	1.6	4.8	C1
onshore	-10	20	0.28	44.51867	-124.271	23.33	8	259	30	0.03	1.4	1.9	C1
onshore	-10	40	0.31	44.68333	-124.27383	25.94	8	287	28.7	0.09	4.3	0.9	D1
onshore	-30	-60	-0.07	43.88283	-124.56783	29.21	8	283	44.2	0.04	1.6	0.4	C1
onshore	-30	-40	0.4	44.04883	-124.52617	26.35	8	266	50.7	0.06	2.6	3.9	D1
onshore	-30	-20	-0.01	44.19917	-124.53933	32.11	8	264	63.5	0.1	4.8	6	D1
onshore	-30	0	1.06	44.346	-124.45433	24.99	8	260	52.2	0.07	1.8	3.6	C1
onshore	-30	20	1.36	44.4795	-124.443	25.63	8	270	44.3	0.16	5.8	8.2	D1
onshore	-30	40	1.01	44.63117	-124.505	27.72	8	291	46.2	0.15	8.1	1.6	D1
onshore	-50	-60	1.15	43.89717	-124.67083	33.93	8	288	52.6	0.24	10.1	1.8	D1
onshore	-50	-40	2.19	44.07717	-124.5775	25.68	8	270	55.8	0.17	2.2	3.4	C1
onshore	-50	-20	1.27	44.199	-124.62983	32.61	8	273	68.2	0.05	2.3	0.5	C1
onshore	-50	0	0.75	44.34417	-124.69133	26.6	8	281	68.5	0.23	5.5	1.3	D1
onshore	-50	20	2.23	44.44617	-124.55967	28.62	8	277	54.3	0.21	8.8	2.1	D1
onshore	-50	40	4.14	44.49867	-124.46567	11.96	8	274	45.3	0.34	6.7	25	D1
onshore	-70	-60	3.12	43.97317	-124.68833	28	8	285	57	0.34	16.7	4.4	D1
onshore	-70	-40	3.4	44.0995	-124.63233	30.29	8	275	60.8	0.28	11.9	4.8	D1
onshore	-70	-20	2.49	44.19	-124.707	26.59	8	280	71.9	0.22	1.4	2.2	C1
onshore	-70	0	2.41	44.323	-124.71967	28.43	8	283	71.6	0.15	5.2	1	D1
onshore	-70	20	3.41	44.42533	-124.64283	28.18	8	281	61.3	0.21	9.8	2.2	D1
onshore	-70	40	5.4	44.4815	-124.53717	11.96	8	278	51.3	0.33	5	21.1	D1
onshore	-90	-60	4.87	44.00133	-124.7585	11.98	8	288	63.4	0.43	5.3	22.7	D1
onshore	-90	-40	3.75	44.11167	-124.81167	28.53	8	288	73.2	0.21	9.2	1.8	D1
onshore	-90	-20	4.16	44.19167	-124.76267	26.49	8	284	75.4	0.23	1.6	2.5	C1
onshore	-90	0	4.13	44.313	-124.77183	30.69	8	286	75.8	0.1	4.9	1.2	D1
onshore	-90	20	6.46	44.368	-124.59617	14.93	8	275	60.5	0.4	15.3	52.5	D1
onshore	-90	40	6.89	44.46083	-124.59967	11.97	8	281	56.7	0.33	4.5	21	D1

Table 2.

June 21, 2012

Crustal Model	Vp/Vs Ratio	Latitude	Longitude	Depth (km)	RMS	Horizontal Error	Vertical Error	Number of Picks
OR3	1.77	44°25.47' N	124°32.70' W	14.82	0.23	1.2	1.2	24
OR3	1.78	44°25.30' N	124°32.17' W	15.82	0.22	1.1	0.8	24
OR3	1.84	44°24.40' N	124°28.13' W	20.05	0.22	1.0	0.9	24
OR3	1.90	44°23.35' N	124°23.57' W	21.57	0.25	1.2	0.9	24
CR	1.77	44°26.21' N	124°34.46' W	30.53	0.25	1.4	2.1	24
CR	1.78	44°25.79' N	124°32.69' W	31.93	0.24	1.4	2.1	24
CR	1.84	44°25.32' N	124°29.18' W	30.64	0.21	1.1	1.4	24
CR	1.90	44°23.95' N	124°24.32' W	31.41	0.24	1.3	1.5	24

June 28, 2012

Crustal Model	Vp/Vs Ratio	Latitude	Longitude	Depth (km)	RMS	Horizontal Error	Vertical Error	Number of Picks
OR3	1.74	44°36.33' N	124°17.25' W	14.94	0.45	0.9	1.1	60
OR3	1.78	44°36.29' N	124°16.32' W	14.76	0.42	0.7	0.8	61
OR3	1.84	44°35.81' N	124°15.57' W	14.93	0.51	0.9	0.9	61
CR	1.74	44°37.28' N	124°20.47' W	28.12	0.37	0.8	1.0	60
CR	1.78	44°36.73' N	124°19.18' W	27.07	0.28	0.6	0.9	60
CR	1.84	44°35.92' N	124°17.28' W	23.31	0.30	0.6	1.0	61

June30, 2012

Crustal Model	Vp/Vs Ratio	Latitude	Longitude	Depth (km)	RMS	Horizontal Error	Vertical Error	Number of Picks
OR3	1.78	44°36.35' N	124°16.77' W	14.50	0.41	0.8	0.7	61
OR3	1.84	44°36.09' N	124°15.86' W	16.03	0.48	0.9	0.9	61
OR3	1.90	44°35.29' N	124°14.56' W	16.45	0.66	1.2	1.2	61
CR	1.78	44°36.97' N	124°18.81' W	28.44	0.24	0.5	0.7	59
CR	1.84	44°36.00' N	124°17.14' W	24.47	0.30	0.6	0.9	60
CR	1.90	44°35.28' N	124°16.04' W	21.53	0.44	0.8	1.4	61